Seasonal patterns of canopy photosynthesis captured by remotely sensed sun-induced fluorescence and vegetation indexes in mid-to-high latitude forests: A cross-platform comparison.

Xinchen Lu[1], Xiao Cheng[1, 2*], Xianglan Li[1, 2*], Jiquan Chen[3], Minmin Sun[1], Ming Ji[1], Hong He[1], Siyu Wang[1], Sen Li[1] and Jianwu Tang[4]

[1]State Key Laboratory of Remote Sensing Science, College of Global Change and Earth System Science, Beijing Normal University, Beijing 100875, China

[2]Joint Center for Global Change and China Green Development, Beijing Normal University, Beijing 100875, China

[3] College of Social Science, Department of Geography, Michigan State University, East Lansing, Michigan, USA

[4]The Ecosystems Center, Marine Biological Laboratory, Woods Hole, Massachusetts, USA

Correspondence and request of materials should be addressed to Xiao Cheng (xcheng@bnu.edu.cn) and Xianglan Li (xlli@bnu.edu.cn)

Abstract

Characterized by the noticeable seasonal patterns of photosynthesis, mid-to-high latitude forests are sensitive to climate change and crucial for understanding the global carbon cycle. To monitor the seasonal cycle of the canopy photosynthesis from space, several remote sensing based indexes, such as normalized difference vegetation index (NDVI), enhanced vegetation index (EVI) and leaf area index (LAI), have been implemented within the past decades. Recently, satellite-derived sun-induced fluorescence (SIF) has shown great potentials of providing retrievals that are more related to photosynthesis process. However, the potentials of different canopy measurements have not been thoroughly assessed in the context of recent advances of new satellites and proposals of improved indexes. Here, we present a cross-site intercomparison of one emerging remote sensing based index of phenological index (PI) and two SIF datasets against the conventional indexes of NDVI, EVI and LAI to capture the seasonal cycles of canopy photosynthesis. NDVI, EVI, LAI and PI were calculated from Moderate Resolution Imaging Spectroradiometer (MODIS) measurements, while SIF were evaluated from Global Ozone Monitoring Experiment-2 (GOME-2) and Orbiting Carbon Observatory-2 (OCO-2) observations. Results indicated that GOME-2 SIF was highly correlated with gross primary productivity (GPP) and absorbed photosynthetically active radiation (APAR) during the growing seasons. Key phenological metrics captured by SIF from GOME-2 and OCO-2 matched closely with photosynthesis phenology as inferred by GPP. However, the applications of OCO-2 SIF for phenological studies may be limited only for a small range of sites (at site-level) due to a limited spatial sampling. Among the MODIS estimations, PI and NDVI provided most reliable predictions of start of growing seasons, while no indexes accurately captured the end of growing seasons.

Keywords: *Phenology, remote sensing, photosynthesis, OCO-2, SIF, NDVI, EVI, PI, LAI.*

1. Introduction

Terrestrial ecosystems play an important role in regulating regional and global climate (Burrows et al., 2011). Mid-to-high latitude forests, especially the boreal forests, are

substantial contributors to carbon fluxes (Beer et al., 2010; Rolleston, 1996). As plants in these regions are expected to experience the greatest warming among forest biomes, they are deemed to react and respond sensitively to climate change and variability (Kurz et al., 1995). Despite the important roles of mid-to-high latitude forests in the global carbon cycle, it remains challenging to monitor and model the physiological processes such as photosynthesis.

Mid-to-high latitude forests are showing noticeable seasonal cycles of photosynthesis, which are sensitive indicators of the biosphere's response to climate changes through contributions to the global carbon, energy and water cycles (Buitenwerf et al., 2015; Peñuelas et al., 2009). Understanding the changes of these cycles as well as the underlying mechanisms are of significance for predicting future changes of climate and the global carbon cycle. Recent *in-situ* and remote sensing based studies have shown that the warming climate has triggered lengthier growing seasons in northern hemisphere regions (Cleland et al., 2007; Viña et al., 2016; Wang et al., 2015). Remote sensing based approaches to estimate phenological metrics (e.g., the start and end of growing seasons) were mainly based on reflectance-calculated vegetation indexes (VIs), such as normalized difference vegetation index (NDVI), enhanced vegetation index (EVI) and leaf area index (LAI) retrieved using these VIs (Tang et al., 2016). These indexes have been applied to regional and global studies, especially for the regions without long-term ground observations. However, performance of VIs is significantly hindered by snow cover and soil moisture (D'Odorico et al., 2015b; Peng et al., 2017; Wu et al., 2017). Several improved indexes including phenological index (PI) that aimed at the matches between remotely sensed and ground observed seasonal cycles of canopy photosynthesis have been proposed. PI combines NDVI and Normalized Difference Infrared Index (NDII) to decouple the seasonality of the green vegetation component from that of the background because green-up co-occurs with snow melt (Delbart et al., 2005; Gonsamo et al., 2012a). Yet, the biological recovery and dormancy of trees for evergreen forests are still extremely difficult to identify during the transition period when the greenness

signal of the vegetation is weak or does not necessarily correspond with the shifts of photosynthesis (Wong and Gamon, 2015).

Alternatively, chlorophyll pigments absorb photons to power photosynthesis, with some of the photons re-emitted at longer wavelengths as chlorophyll fluorescence (Baker, 2008). The re-emitted sun-induced fluorescence (SIF) has been successfully related to downward carbon flux, i.e., carbon uptake by the vegetation. This provides a promising way in estimating photosynthesis through SIF. Global SIF datasets using space-borne spectroscopy from satellites became available past few years (Frankenberg et al., 2014; Guanter et al., 2013; Guanter et al., 2014; Joiner et al., 2013; Joiner et al., 2016; Köhler et al., 2015). Despite the complex processes underlying the relationships between SIF and gross primary production (GPP), it has been reported the satellite-retrieved SIF was highly correlated with GPP estimated based on eddy covariance (EC) flux towers (van der Tol et al., 2014; Yang et al., 2017; Yang et al., 2015; Zhang et al., 2016b). Their relationships appear to reflect the level of APAR as well as light use efficiency (LUE). Based on more than 50 global EC towers, Joiner et al. (2014) found that the Global Ozone Monitoring Experiment-2 (GOME-2) SIF retrieved phenological metrics matched closely with that of EC-based estimations despite the imperfect matches of spatial and temporal representativeness. Walther et al. (2016) found that GOME-2 SIF decoupled growing seasons can be up to 8 weeks longer than that captured by EVI. Jeong et al. (2017) evaluated remotely sensed SIF and NDVI of several platforms and proposed that the continued measurements of SIF and NDVI would help us understand the seasonal variations of vegetation photosynthesis and greenness. However, the coarse spatial representativeness of previous atmospheric measurements (~ 40 km by 80 km or coarser) makes it difficult to compare with ground-based canopy measurements (Chen et al., 2012; Joiner et al., 2014; Zhang et al., 2016b). Very recently, Orbiting Carbon Observatory (OCO-2) has shown renewed promises of satellite-derived fluorescence with the improved spatial representativeness at around 1.3 km by 2.25 km (Frankenberg et al., 2014; Sun et al., 2017). The similar footprints of OCO-2 that match the spatial representativeness of most EC towers enables it to produce more sounding results (Lu et al., 2018; Verma et al., 2017). The

emerging observations from OCO-2, however, have rarely been applied in phenological studies (Köhler et al., 2017).

Our primary objective is to evaluate and compare the seasonal cycles of several remotely sensed canopy measurements. An additional objective is to focus on phenological transition dates derived from different measurements, which are indicators directly related to the carbon budgets of terrestrial ecosystems.

2. Materials and Methods

2.1 Selection of EC sites

We conducted this study at 15 EC sites (103 site-years) in North America and Europe where relatively homogeneous landscapes exist around the flux towers. These sites represent three main forest biomes in mid-to-high latitude forests such as evergreen needleleaf forests (ENF), deciduous broadleaf forests (DBF) and mixed forests (MF) (Fig. 1 and Table 1). The selection of EC sites was based on an assumption of threshold of International Geosphere-Biosphere Program (IGBP) classifications (Loveland et al., 2000). In principle, we chose sites where >60% of the GOME-2 grid areas around each flux tower matched with the biome for the corresponding site. MODIS land cover products (MCD12Q1) and previous studies on several homogeneous sites were used as references for our site selection (Zhang et al., 2016a). For some sites, MODIS grids classified as mixed forests around the tower were not distinct from ENF or DBF grids. EC measurements were downloaded from the European Fluxes Database Cluster (http://gaia.agraria.unitus.it/) and Fluxnet (http://fluxnet.fluxdata.org/).

We used gap-filled including air temperature, downward shortwave radiation (SWIN) and CO_2 fluxes. The daily composites were resampled every 8 days with an average over the 16-day period. Quality flags and/or standard errors were screened for all analysed parameters to ensure that only the most reliable estimations remained. Photosynthetically active radiation (PAR) was calculated as 0.45 of SWIN for all sites. The conversion factor of 0.45 has been widely applied in cross-site studies (Jin et al., 2015). To partition net ecosystem exchange

(NEE) into GPP and ecosystem respiration, we follow the night-time partitioning method (Reichstein et al., 2005).

A modelling estimations of GPP with the same spatial representativeness of GOME-2 SIF from FLUXCOM were referred to in this study (Jung et al., 2009; Tramontana et al., 2016). Based on remote sensing and meteorological data, this set used several machine-learning algorithms to upscale flux tower estimations to the global scale. The seasonal cycles of this dataset have been proved to be correlated with ground observations (Tramontana et al., 2016). We averaged the outcomes of six algorithms , i.e., three machine-learning algorithms by two partitioning methods, and then resampled the composites every 8 days with an average over the 16-day period.

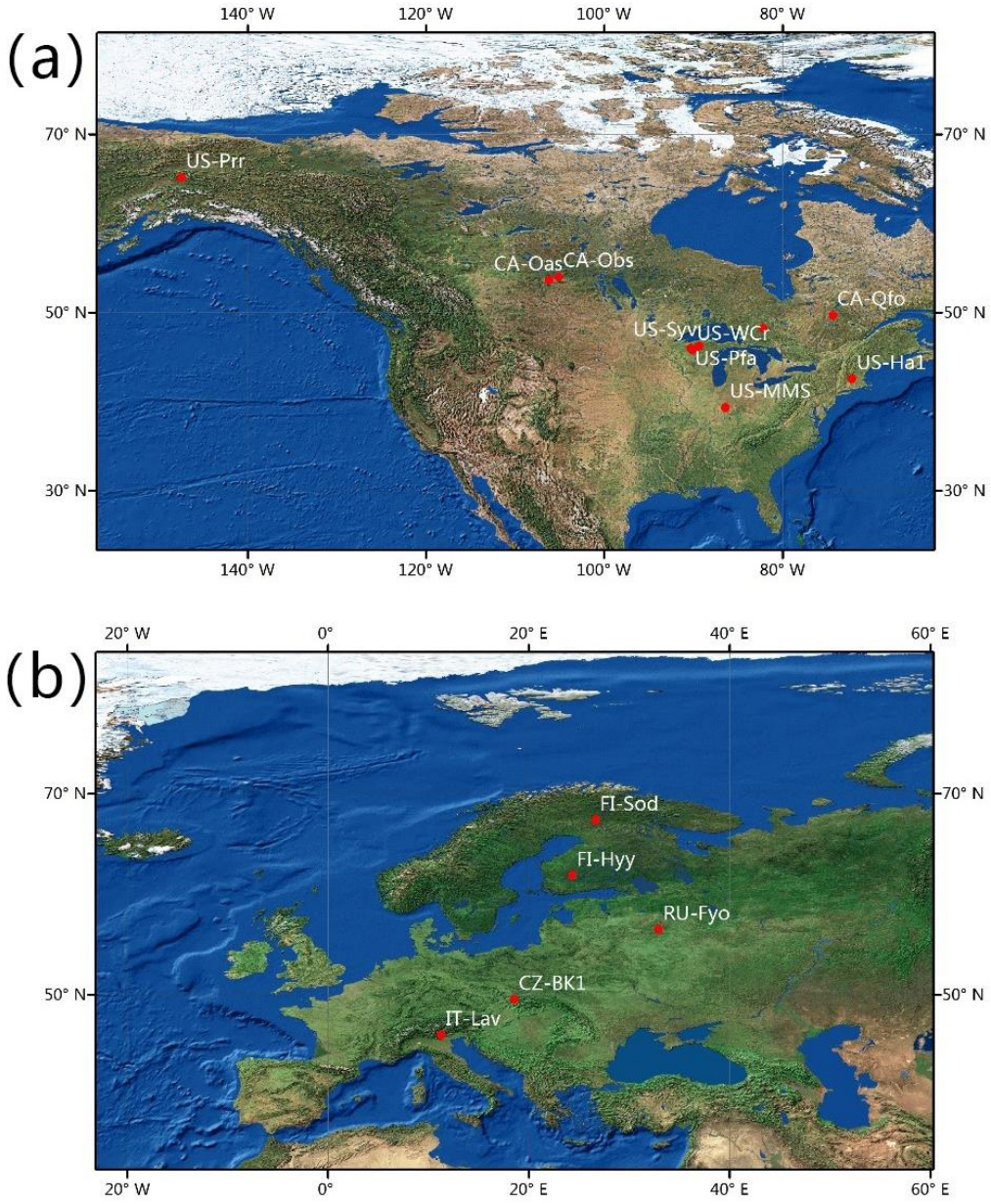

Figure 1. Spatial distributions of the 15 mid-to-high latitude forests in North America (a) and Europe (b). The figure was generated using ArcMap 10.2 (http://www.esri.com/).

Table 1. Basic information and descriptions of EC flux sites. Among all sites, eddy measurements of sites CZ-BK1, DK-Sor, FI-Sod, IT-Lav, and RU-Fyo were downloaded from the European Fluxes Database Cluster, while measurements from other sites were obtained from the FLUXNET. Year denotes the corresponding time of the measurements, Type indicates land cover type, and Max_LC is the percent of dominant vegetation cover within the GOME-2 grid calculated for each site. OCO-2 indicates whether this site was selected for comparisons with OCO-2 measurements.

Site	Lat.	Lon.	Site Name	Year	Type	Max_LC	OCO-2	References
CA-Gro	48.2167	−82.1556	Canada-Ontario 4	2007–2014	MF	90	Yes	Mccaughey et al. (2006)
CA-Oas	53.6289	−106.1978	SK-Old Aspen	2007–2010	DBF	60	Yes	Barr et al. (2002)
CA-Obs	53.9872	−105.1178	SK-Southern Old Black Spruce	2007–2010	ENF	88	No	Bond-Lamberty et al. (2004)
CA-Qfo	49.6925	−74.3421	Eastern Boreal, Mature Black Spruce	2007–2010	ENF	71	No	Bergeron et al. (2007)
CZ-BK1	49.5021	18.5369	Bily Kriz- Beskidy Mountains	2007–2014	DBF	60	No	Staudt and Foken (2008)
FI-Hyy	61.8475	24.295	Finland-Hyytiala	2007–2014	ENF	93	No	Suni et al. (2003)
FI-Sod	67.3619	26.6378	Sodankyla	2007–2014	ENF	99	No	Tanja et al. (2003)
IT-Lav	45.9562	11.2813	Italy-Lavarone	2007–2014	ENF	60	Yes	Marcolla et al. (2003)
RU-Fyo	56.4615	32.9221	Russia-Fyodorovskoye dry spruce	2007–2014	ENF	95	Yes	Milyukova et al. (2002)
US-Ha1	42.5378	−72.1715	Harvard Forest EMS Tower (HFR1)	2007–2012	DBF	91	No	Urbanski et al. (2007)
US-MMS	39.3232	−86.4131	Morgan Monroe State Forest	2007–2014	DBF	91	No	Dragoni et al. (2011)
US-PFa	45.9459	−90.2723	USA-Park Falls	2007–2014	MF	78	Yes	Desai (2014)
US-Prr	65.1237	−147.4876	Poker Flat Res. Range Black	2010–2014	ENF	87	No	Nakai et al. (2013)

			Spruce					
US-Syv	46.242	−89.3477	USA-Sylvania Wilderness Area	2007–2014	MF	93	No	Desai et al. (2005)
US-WCr	45.8059	−90.0799	USA-Willow Creek	2007–2014	DBF	95	Yes	Cook et al. (2004)

2.2 Satellite-derived SIF

We used satellite-derived SIF data derived from the GOME-2 instrument on-board MetOp-A platform (ftp://fluo.gps.caltech.edu/data/Philipp/GOME-2) which initially measured backscattered sunlight in a nadir-viewing geometry at wavelengths between 270 and 790 nm in four separate channels. Its fourth channel (590-790 nm) encompassed a range of wavelengths of emitted SIF. This dataset used a linear method to retrieve SIF at 740 nm (Köhler et al., 2015). The SIF dataset was gridded with a spatial resolution of 0.5 degrees after normalizing to the daily averages. We regridded daily retrievals centered at each site using the bilinear interpolation algorithm (Press et al.). Then the daily estimations were resampled every 8 days with an average over the 16-day. As expected, the spatial representativeness of GOME-2 SIF data mismatched with that of most EC towers. Consequently, we applied the remotely sensed fluorescence from OCO-2 that was launched on July 2, 2014. The relatively small footprints of instruments of OCO-2 (~1.3 km by 2.25 km) made it possible to produce the first satellite-derived SIF dataset that better matches with the EC-based estimations. Since OCO-2 has spectrally high resolved measurements in the O_2 A-band, it is capable of retrieving SIF centered at 757 nm and 771 nm accurately (Frankenberg et al., 2014). The SIF at 771 nm is relatively weaker than that at 757 nm, thus we averaged the records of two bands after scaling the values at 771 nm with a factor of 1.4 (Verma et al., 2017).

There are several differences between satellite-derived SIF from the two instruments. Firstly, the retrieved SIF centered at 740 nm for GOME-2 and 757 nm (771 nm) for OCO-2. Secondly, unlike the global continuous measurements of GOME-2, the strategies of spatial sampling of OCO-2 are sparse, with only a few sites in this study to have sufficient times of overpass that can be used to quantify the seasonal patterns. Additionally, the overpass times of the two satellites differ from each other, i.e., morning for GOME-2 and noon for OCO-2. As results, only 6 EC sites with most observations from OCO-2 were selected for comparisons (Table 1). The search radius of OCO-2 SIF data was set at 10 km following the similar protocols of Verma et al. (2017) and Luus et al. (2017). For OCO-2 SIF, we used the daily correction factor provided within the files to convert the instantaneous values to daily averages. The measurements of FLUXNET and European Flux Data Cluster only updated to

2014 for most sites. We merged the values from OCO-2 from late 2014 to 2016 into a year by the corresponding day of the year of the measurements for comparisons with EC-based estimations in 2014.

2.3 Surface reflectance and FPAR/LAI

To calculate NDVI, EVI and PI, bidirectional reflectance distribution function (BRDF) adjusted surface reflectance derived the MODIS instruments were obtained from Oak Ridge National Laboratory's Distributed Active Archive Center (MCD43A4, V005, with a spatial resolution of 500 m,combined from Terra and Aqua) (Attard et al., 2016). In this data set, the values of reflectance were normalized to nadir, cloud-free, atmospherically corrected measurements based on the bidirectional reflectance distribution function, and were attributed into a 16-day series with a sampling of every 8 days. The MCD43 series data sets used a separate product (MCD43A2) in simplified form to store quality information. The layer of “BRDF_Albedo_Quality” indicated the quality of the BRDF-adjusted reflectance. We only used the measurements labelled as "best" and "good" in quality.

Table 2. A summary of all datasets used in this study. The description, size of footprint, period and references are provided as the references.

Dataset	Description	Footprint	Period	Reference
Fluxnet 2015	Flux measurements at multiple sites	Typically 500 m to 1 km	2007-2014	Baldocchi et al. (2001)
European Flux Database Cluster	Flux measurements at multiple European sites	Typically 500 m to 1 km	2007-2014	Sulkava et al. (2015)
Fluxcom	An upscaled modeling GPP data set	0.5 degrees	2007-2013	Jung et al. (2011)
GOME-2 SIF	Satellite-derived SIF from GOME-2	40 km by 80 km	2007-2014	Köhler et al. (2015)
OCO-2 SIF	Satellite-derived SIF from OCO-2	1.3 x 2.25 km	2014-2016	Frankenberg et al. (2014)
MOD15A2	Level 4 product of FPAR & LAI	1 km	2007-2014	Myneni et al. (2002)
MCD43A4	MODIS Nadir BRDF-Adjusted Reflectance surface reflectance	500 m	2007-2014	Attard et al. (2016)

We used the level 4 product of the Fraction of Photosynthetically Active Radiation (FPAR) and the LAI from the Oak Ridge National Laboratory's Distributed Active Archive Center (MOD15A2, V005, with a spatial resolution of 1000 m, from MODIS Terra) (Fretwell et al., 2012; Myneni et al., 2002). For product MOD15A2, retrievals were targeted towards consistency with field measurements over all biomes but with a major focus on woody vegetation. We resampled the measurements every 8 days with an average over the 16-day.

2.4 Computations of Vegetation Indexes and Phenological Indexes

To proxy green biomass, the red, blue, near-infrared and shortwave-infrared surface reflectance from the MCD43A4 product with the exact acquisition dates were used to compute the EVI, NDVI, and PI. The EVI and NDVI were calculated as (Gonsamo et al., 2012b; Huete et al., 2002; Rouse et al., 1974):

$$\mathrm{EVI} = 2.5 \times \frac{\rho_{nir} - \rho_{red}}{\rho_{nir} + (6 \times \rho_{nir} - 7 \times \rho_{blue}) - 1} \quad (1)$$

$$\mathrm{NDVI} = \frac{\rho_{NIR} - \rho_{red}}{\rho_{NIR} + \rho_{red}} \quad (2)$$

NDVI and NDII were integrated to calculate PI (Delbart et al., 2005; Gonsamo et al., 2012a). NDII responds to land surface moisture and snow cover and can thus capture the seasonal trajectories of snow cover. The PI was derived from the product of the sum and the difference of NDVI and NDII as (Delbart et al., 2005; Gonsamo et al., 2012a):

$$\mathrm{NDII} = \frac{\rho_{NIR} - \rho_{SWIR}}{\rho_{NIR} + \rho_{SWIR}} \quad (3)$$

$$\mathrm{PI} = \begin{cases} 0, \ if \ \ NDVI < 0 \ \ or \ \ NDII < 0 \\ (NDVI + NDII) \times (NDVI - NDII) \\ 0, \ if \ \ PI < 0 \end{cases} \quad (4)$$

2.5 The linear model and hyperbolic model for illustrating the SIF-GPP relationships

The relationships between SIF and canopy photosynthesis can be complex, several previous studies pointed out that their relationships can be nonlinear (Damm et al., 2010; Damm et al., 2015; Li et al., 2017; Yang et al., 2016; Zhang et al., 2016a). Damm et al. (2015) and Li et al. (2017) proposed that a hyperbolic model may outperform the linear model when analysing the relationships between SIF and GPP. In this study, we used the linear model as well as the hyperbolic (nonlinear) model to analyse the relationships between SIF and GPP.

The hyperbolic model assumed that the SIF-GPP relationships can be nonlinear as LUE can be expressed by a hyperbolic function of APAR. This simplified model can be expressed as follow (Li et al., 2017):

$$\mathrm{GPP} = GPP_{max} \times \frac{SIF}{SIF+b} \quad (5)$$

Where GPP_{max} represents the maximum of a GPP dataset and b was a parameter related to SIF_{yield} (SIF divided by APAR).

2.6 Determinations of phenological metrics

We used the curve fitting method to objectively determine phenological metrics (Gonsamo et al., 2012b).

$$X(t) = a1 + \frac{a2}{1+\exp(-d1(t-b1))} - \frac{a3}{1+\exp(-d2(t-b2))} \quad (6)$$

Equation (6) was fitted to all measurements, where $X(t)$ is the input time series (e.g., GOME-2 SIF), and $a1$, $a2$, $a3$, $b1$, $b2$, $d1$, and $d2$ are the empirical coefficients to be estimated. Weighting-scheme based least-squares curve fitting was applied by starting from a first guess of the seven functions and solving with a maximum of 2000 iterations. A four-point moving window approach was used to reduce the effect of low-quality data points by assigning the values less than half or more than twice of its associated median values with lower weights. For NDVI, we referred to the midpoints of b1 and b2 as the start of seasons (SOS) and end of seasons (EOS) as previous studies found that the midpoint-days of NDVI are strongly connected with leaf-unfolding process for deciduous forests in North America and China (D'Odorico et al., 2015a; Luo et al., 2014). For other observations, the phenological metrics were determined as (Gonsamo et al. (2012a):

$$SOS = b1 - \frac{4.562}{2d1} \quad (7)$$

$$EOS = b2 + \frac{4.562}{2d2} \quad (8)$$

Because of the limited observations of OCO-2 SIF, it can be problematic to retrieve 7 free parameters. Based on an assumption that the basing values of SIF at spring and autumn are comparable that should be very close to 0 in theory, we simplified the models by using the same value for a1 and a2 by assuming that the biophysical environments are similar in non-growing seasons.

3. Results

3.1 Relationships between the measurements of GOME-2 SIF and EC towers

The relationships between satellite-derived SIF and canopy photosynthesis during the growing seasons were explored firstly through linear regression analysis (Fig. 2). We found that the seasonal patterns of SIF correlated highly with EC-based estimations of GPP (GPP_{EC}), with the correlation coefficient of determination (R^2) ranged from 0.53 to 0.74. Despite our efforts in identifying the EC sites with relatively homogeneous landscapes around the tower, the GOME-2 SIF products were generated within the huge grids. Because the GOME-2 SIF and upscaled GPP ($GPP_{upscaled}$) have the similar spatial representativeness, relatively higher average R^2 values ranging from 0.63 to 0.74 occurred in this study (compared with correlations between SIF and GPP_{EC}). Finally, SIF correlated well with APAR (MODIS FPAR×PAR), with the R^2 ranging from 0.41 to 0.59.

Then, we applied the hyperbolic model to estimate the relationships between GOME-2 SIF and canopy photosynthesis (Fig. 2). In all cases, interestingly, the hyperbolic outperformed the linear model slightly. The coefficients of determination showed an increase of 0.08 to 0.27 when using the hyperbolic model. Especially, when looking at the relationships between SIF and $GPP_{upscaled}$ in DBF and MF, a linear model seems to be inappropriate since there existed obvious saturation effects of photosynthesis in $GPP_{upscaled}$ for DBF and MF when comparing against SIF.

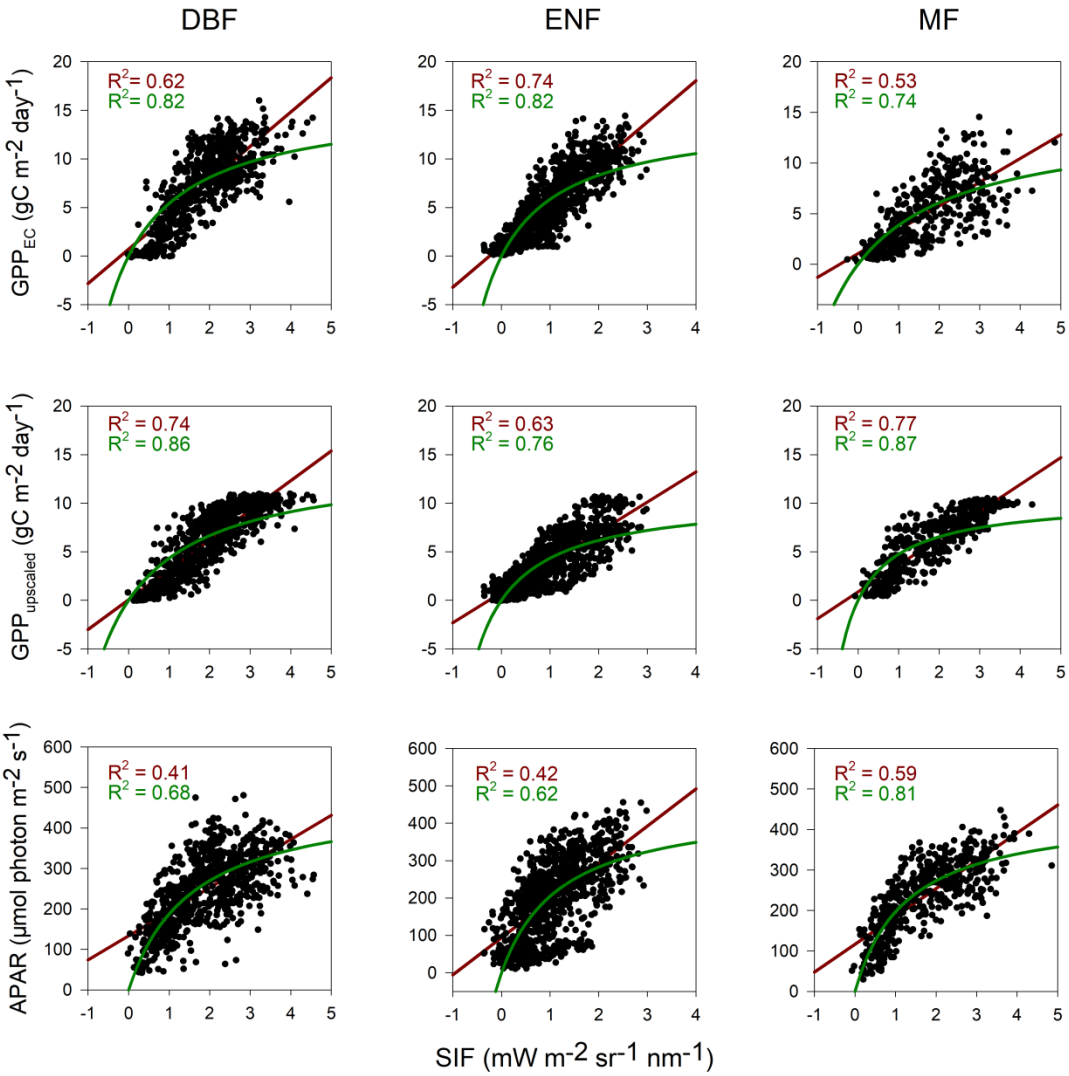

Figure 2. Seasonal correlations between GOME-2 SIF and canopy photosynthesis in different forest biomes. The red line represents the linear model, while the green line shows the hyperbolic model. The coefficients of determination of linear (red texts) and hyperbolic models (green texts) are remarked.

The seasonal trajectories of SIF, GPP_{EC}, PAR, APAR, and EVI×PAR with averaged and normalized values for all sites are shown in Fig. 3. SIF and GPP_{EC} showed closed spring onset and autumn senescence/abscission. However, APAR had relatively different seasonal trajectories from SIF, with an earlier spring onset. For autumn senescence/abscission, SIF, GPP_{EC}, and APAR seemed to cease at a similar time (e.g., CA-Oas and CA-Obs). Since the estimations of APAR based on MODIS FPAR seemed imperfect, we used an alternative method to quantify APAR based on MODIS-derived EVI (Liu et al., 2017; Xiao et al., 2004a;

Xiao et al., 2004b). This method used EVI to estimate the seasonal cycles of chlorophyll absorbed PAR. We found that EVI×PAR showed a seasonal cycle that was more consistent with GPP_{EC} and SIF (e.g., US-Syv).

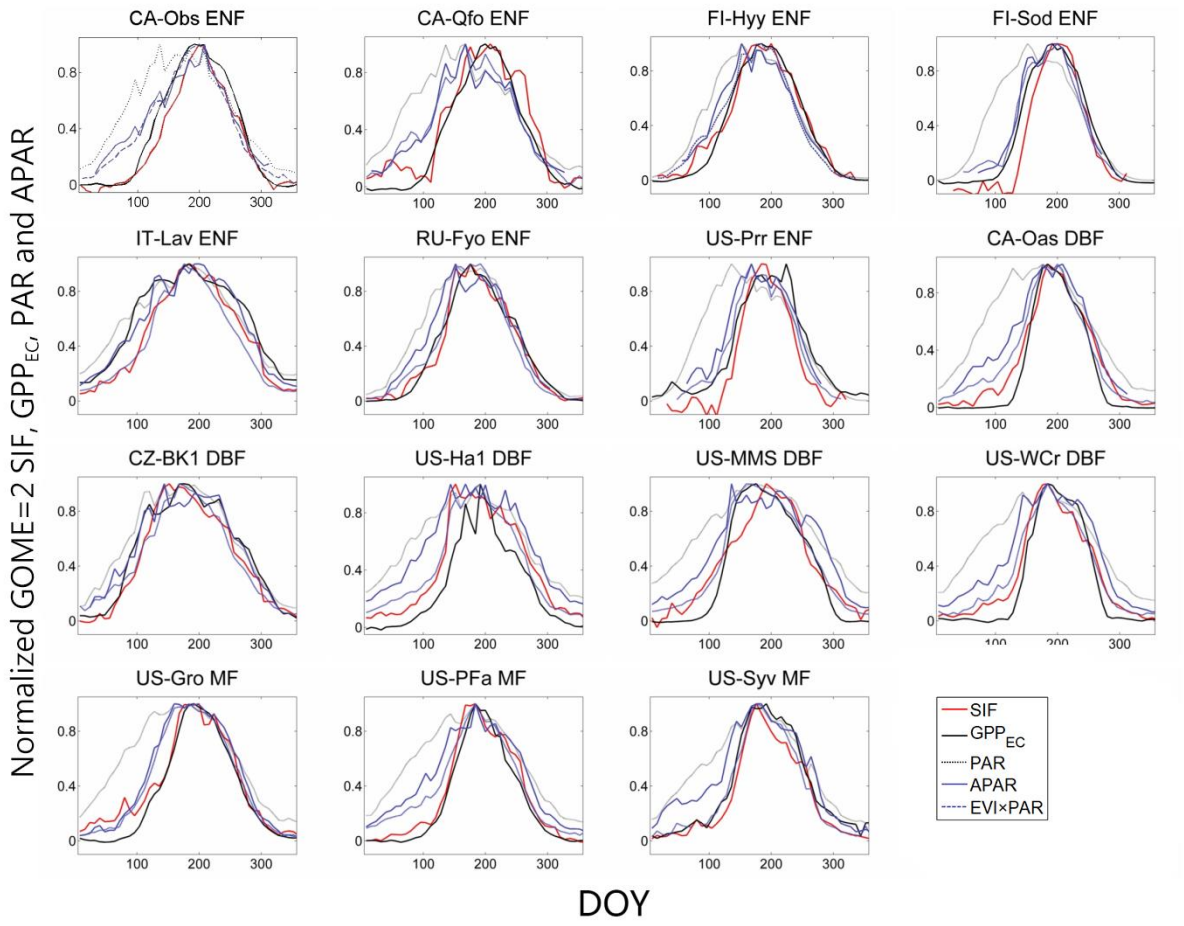

Figure 3. Seasonal trajectories of normalized GOME-2 SIF, PAR, APAR, EVI×PAR, and GPP_{EC} of the 15 sites.

3.2 Phenological metrics captured by different satellites

Although GOME-2 SIF datasets had mismatched spatial representativeness compared with tower-based estimations, we speculated that SIF-captured phenological metrics can be used as a reference indicator of the spring and autumn dynamics at a large-scale.

Results indicated that SOS and EOS derived using VIs, LAI and SIF were comparable but not equivalent (Figs. 4 and 5). Overall, the estimations of all remotely sensed approaches were significantly correlated with that determined by GPP_{EC} ($p<0.05$). For both the start and end of growing seasons, GOME-2 SIF provided the most reliable estimations, with highest R^2 (0.67 for SOS and 0.52 for EOS) and lowest RMSEs (12.36 days for SOS and 11.64 days for

EOS). The regression slope was more close to 1 as well. For the other four MODIS based indexes, the remotely sensed phenological metrics and EC estimated seasonal cycles showed weaker correlations, with the overall R^2 <0.4. For delineating the start of growing seasons, MODIS NDVI and PI had most accurate predictions (R^2 were 0.46 and 0.43 respectively). Other MODIS based indexes showed less promising results, with an overall R^2 below 0.3. For autumn onset, the remotely sensed vegetation indexes seemed to be humped, with the R^2 of <0.1 for MODIS NDVI, and R^2 of < 0.4 for other indexes.

In DBF, GOME-2 SIF tracked the spring onset and autumn senescence/abscission accurately (Fig. 5). Both GOME-2 SIF and EC based estimations of GPP_{EC} showed that the growing seasons started from early-to-middle April and ceased in late October, with PI and NDVI tended to predict longer growing seasons. In ENF, SIF produced a later spring onset by a few weeks but tracked the autumn senescence/abscission accurately. PI and NDVI seemed to match the growing seasons, while EVI predicted longer growing seasons. In MF, both SIF and PI matched the spring onset and autumn senescence/abscission. For both ENF and DBF, MODIS LAI yielded shorter growing seasons.

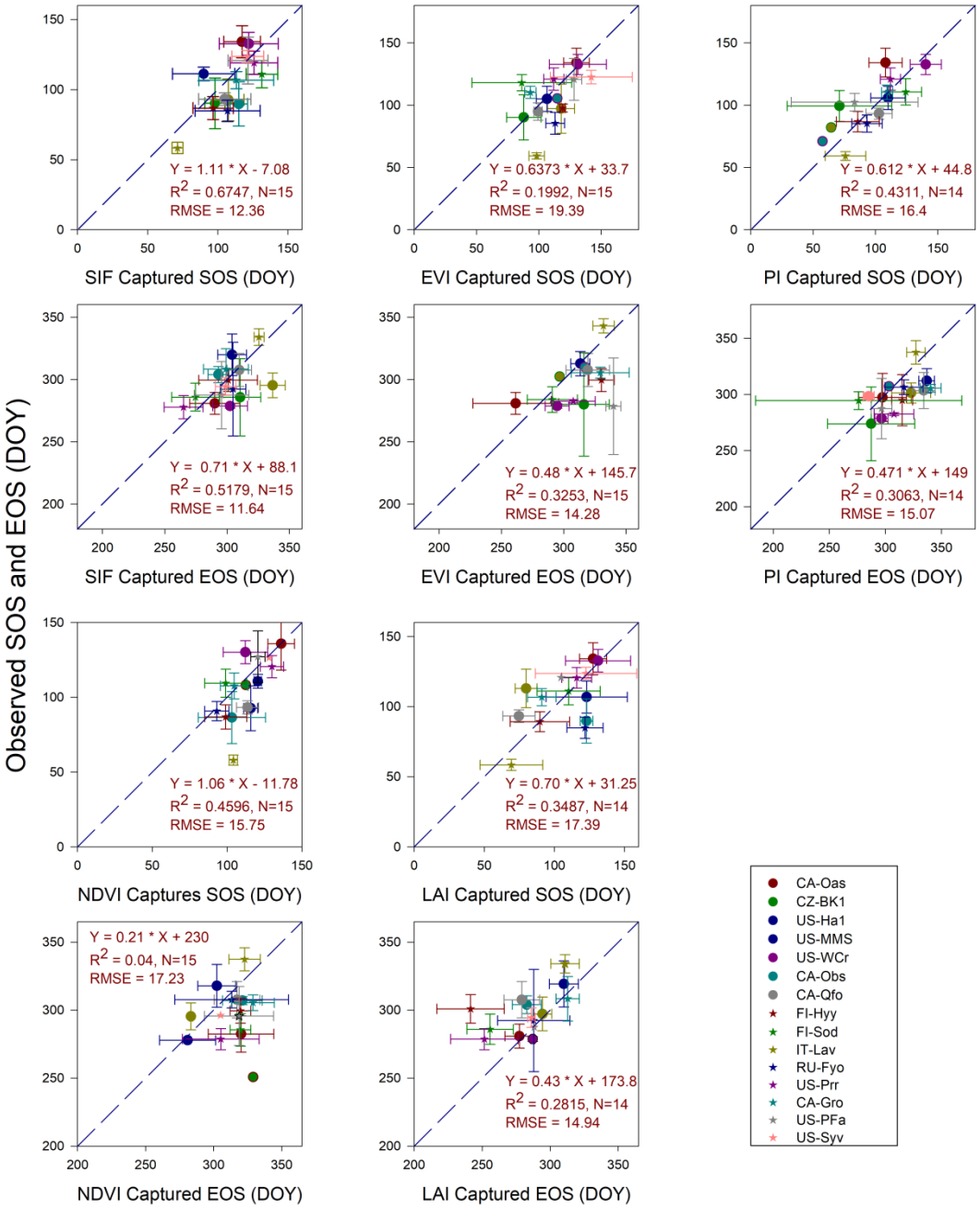

301

302 **Figure 4.** Relationships between remotely sensed phenological metrics and observed
303 photosynthesis metrics determined by EC measurements. The equations and correlation
304 coefficients of determination are shown. The number of sites used (N) and the RMSEs of the
305 linear regressions are also provided for each site, and the error bars are the standard
306 deviations of interannual variations. The absence of error bars indicates that the approaches
307 shared only one year of retrievals, and dashed lines represent the 1:1 lines.

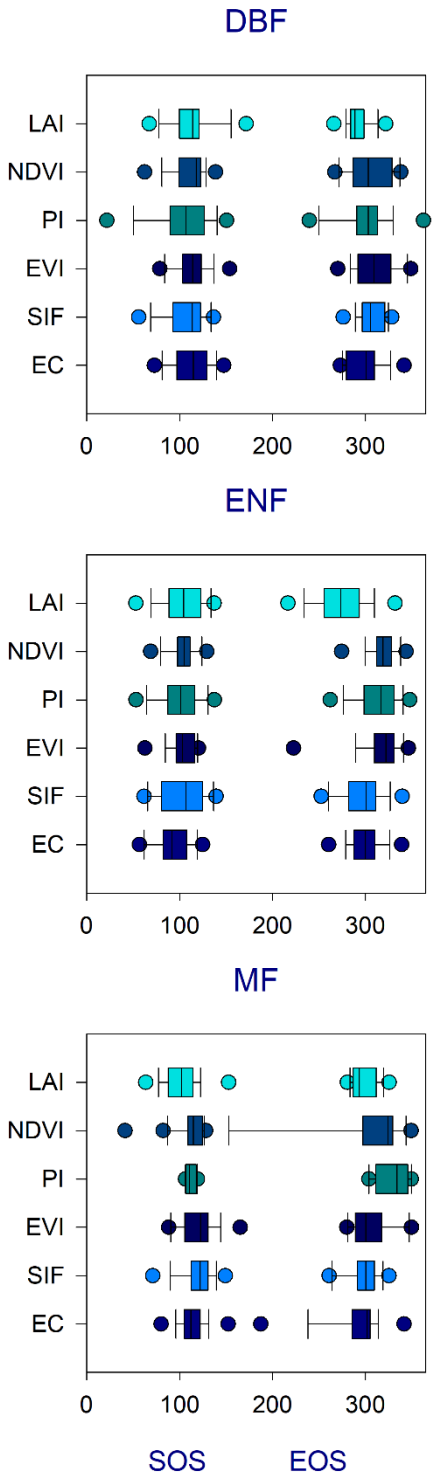

Figure 5. The start and end of the growing seasons determined by different remote sensing measurements and EC measurements. For each data source, the central mark represents the median values, the edges of the box are the 25th and 75th percentiles, and the whiskers extend to the most extreme data points, i.e., 5th and 95th percentiles, that were not

considered.

We found that OCO-2 SIF captured phenological metrics were close to that of GPP_{EC} (Fig. 6). For most sites, OCO-2 SIF captured SOS and EOS matched closely with EC-based estimations, with the onset of spring and autumn within 10 days. However, the OCO-2 inferred growing seasons were generally shorter than that inferred by GPP_{EC}. At in some cases, the seasonal cycles fitted by the double-logistic curve fitting methods were not consistent exactly with that of GPP_{EC} (see US-WCr).

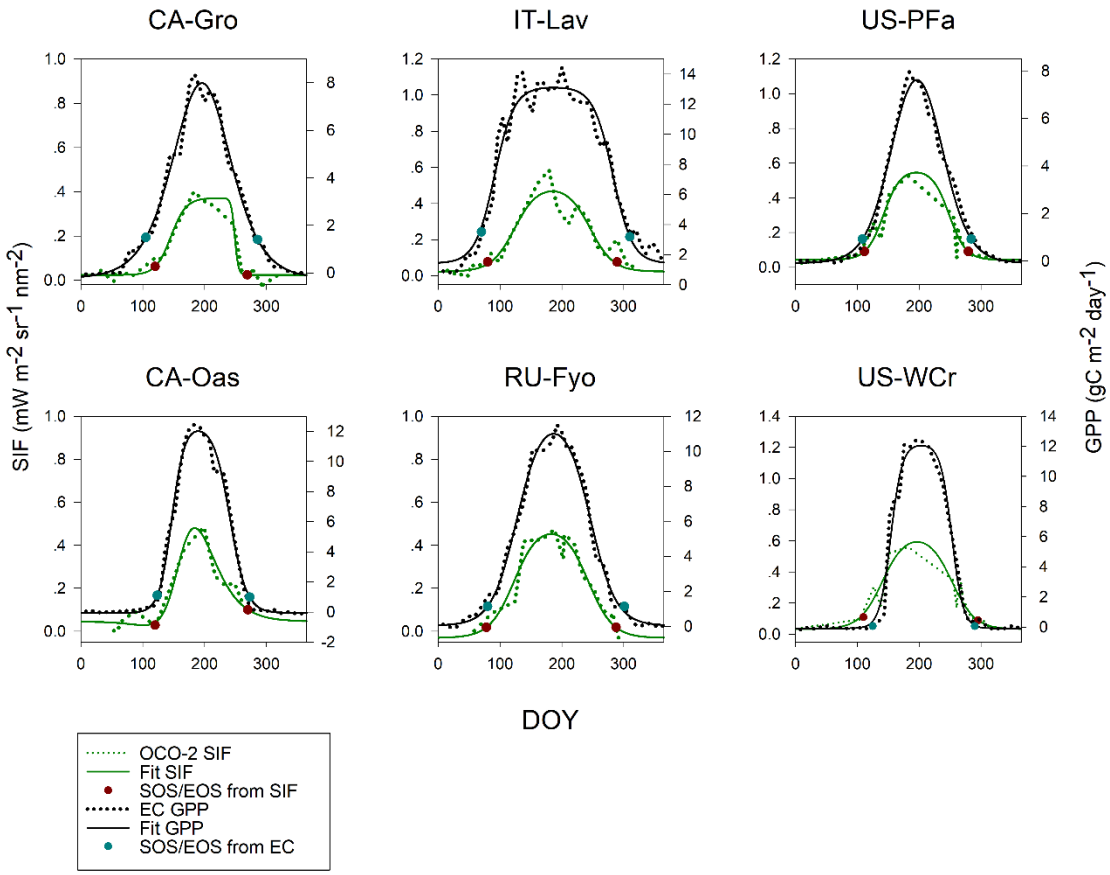

Figure 6. The original measurements, fitted seasonal cycles, and start/end of growing seasons derived from OCO-2 SIF and EC measurements.

4. Discussions

4.1 Uncertainties and Limitations

In this study, we focused on 15 EC sites in mid-to-high latitude forests in Europe and North America to examine the seasonal trajectories of satellite-derived VIs, LAI and SIF, as well as their relationships with EC-based estimations of canopy photosynthesis. An additional

objective is to explore the capacities of five remote sensing based measurements to track the key seasonal metrics in photosynthesis. The uncertainties and limitations of the results are mainly attributed to the following two aspects.

Firstly, the imperfect matches of spatial or temporal representativeness of satellite observations and EC estimations may affect the results. We acknowledge the inherent difficulties when comparing the relatively small spatial scales of tower-based estimations with those of the coarse resolutions of GOME-2 SIF. Although we selected sites with relatively homogenous forests, our assumption that the flux sites can represent the biophysical environment and vegetation of the whole girds may hinder the outcome and reliability of our work (Zhang et al., 2016a). Consequently, we used the modelling GPP that matched the spatial scales of the GOME-2 SIF data as references and explored the emerging OCO-2 SIF at significant improved spatial resolutions that are similar to EC-based estimations (Verma et al., 2017). While the improved spatial representativeness of OCO-2 measurements, the sparse spatial resampling strategies and masks of cloudy measurements lead to limited observations for most sites, which makes it hard to apply them for retrieving seasonal patterns. In this study, we proposed a 2-year (or 3-year) merges of remotely sensed fluorescence from OCO-2 and to analyse the shifts of seasonal photosynthesis patterns based on them. Similar assumptions that the seasonal cycles of a site at different years can be seen alike when comparing cross-site were made in Joiner et al. (2014). Since we exploited a two-year merged SIF sets to extract the underlying seasonal cycles and compared it against EC-based estimations of one year, it might lead to a slight discrepancy of seasonalities.

Secondly, optical remote sensing in high latitudes is relatively humped. Influences of high sun-zenith angles, atmospheric effects, snow cover and repeated observations in the visible bands are obvious and the observations are often complicated by persistent cloud cover. Hence we used the MODIS nadir BRDF adjusted reflectance products in this study because it provides the estimations that are normalized to nadir, cloud-free, and atmospherically corrected.

4.2 SIF-GPP relationships

Despite the potentials of SIF to estimate GPP at various spatial and temporal scales, the

models that can be used for estimating GPP with SIF can be complex and ecosystem-specific (Damm et al., 2015). The relationships between SIF and GPP may contain the information of canopy structure as well as the physiological processes (Badgley et al., 2017). Several studies proposed that the use of a nonlinear model may be more appropriate in some cases (Damm et al., 2010). Zhang et al. (2016a) found that SIF tends to be non-linearly related to GPP at instantaneous time scale, however, their relationships tend to linearize on daily to seasonal scales. In this study, we found that, even on the biweekly scale, the use of a hyperbolic model still outperformed the linear model when illustrating the SIF-GPP relationships. The nonlinear relationships between SIF and GPP were assumed as LUE may be non-linearly responded to APAR.

On seasonal scales, we compared the patterns in averaged GPP_{EC}, SIF and APAR of 15 sites (Fig.7) and found close matches between SIF and GPP_{EC}. The distinct trajectories between APAR and SIF yet existed. While SIF was a direct response to absorbed radiation, the fact that SIF and APAR had distinct seasonal cycles may suggest that SIF of mid-to-high latitude forests was not only driven by APAR but may also be affected by other factors (e.g., light use efficiency). Similar results were found in Walther et al. (2016). Since we used estimated daily SIF against the MODIS based estimations that are usually observed at instantaneous scale, it is accepted that this protocol may affect the results, although VIs of a canopy show less significant variations within a day (Zhang et al., 2018). The models that we used to estimate APAR may also impact the results. Relatively, EVI proxied APAR (EVI×PAR) showed a seasonal pattern more consistent with SIF and GPP_{EC}. This is the reason for us to apply EVI proxied APAR as another estimation of APAR in this study (Turner et al., 2003; Xiao et al., 2004b). Those results are in line with previous results that found EVI being a better proxy of the fraction of chlorophyll absorbed PAR (Liu et al., 2017; Sims et al., 2008).

Additionally, there appeared saturation effects of $GPP_{upscaled}$ for DBF and MF when comparing against SIF. It may be attributed to the fact that Fluxcom used MODIS FPAR for upscaling site-based observations. The performance of MODIS FPAR have been found in previous studies to be hampered by saturation effects (Yang et al., 2015). To produce upscaled datasets of GPP and other parameters, the use of SIF or other improved indexes for

upscaling may further evaluate their performance (Köhler et al., 2017; Tramontana et al., 2016).

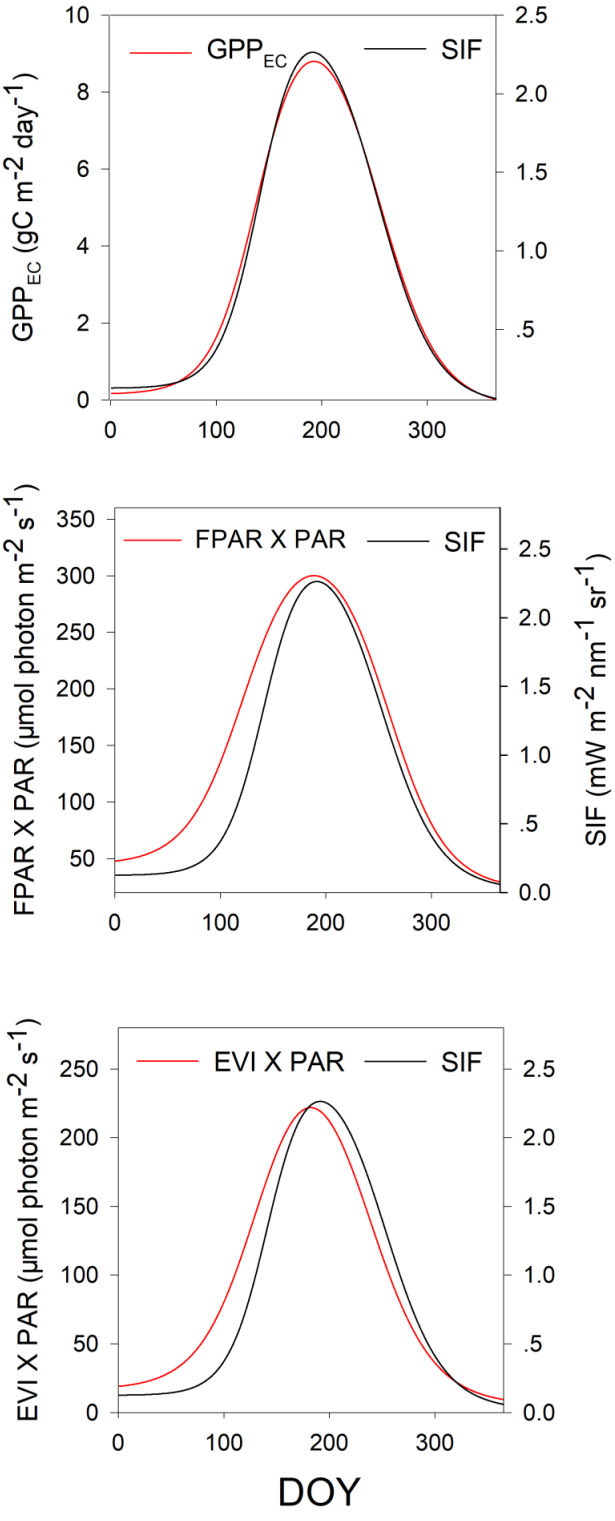

Figure 7. The seasonal cycles of GPP_{EC}, GOME-2 SIF and two estimations of APAR by averaging the outcomes of all sites

4.3 Intercomparison of satellite captured seasonal patterns of canopy photosynthesis

In this study, we compared the potentials of five remote sensing based measurements in predicting seasonal trajectories canopy photosynthesis. Remote sensing based approaches to determine phenological metrics (e.g., SOS and EOS) can be challenging because different parameters may respond uniquely to biophysical environments, resulting in different predictions. We found that, despite the mismatched spatial representativeness of GOME-2 SIF and mismatched observing time of OCO-2 SIF, the seasonal trajectories and phenological metrics depicted by these emerging SIF measurements matched closely with EC-based estimations.

Regardless of our efforts in modelling seasonal cycles from two-year merged sets, the OCO-2 SIF measurements remained limited for most sites. At site-level, the limited numbers of observations will make it extremely difficult to develop seasonal cycles of all sites because only very few sites have sufficient times of observations (Lu et al., 2018). This shortage of data may also be responsible for the relatively shorter growing seasons than that estimated by GPP_{EC} because the weight-based curving fitting method was hindered from determining the free parameters. Thus, at large scales, several studies attempted to generate the monthly means of OCO-2 SIF as the seasonal indicators (Köhler et al., 2017; Luus et al., 2017). The applications of OCO-2 SIF with relatively fine resolutions yet sparse coverages should be carefully deliberated.

5. Conclusions and Outlooks

Our results added additional endorsements for the applications of satellite-derived SIF in phenological studies in forest biomes. In 15 mid-to-high latitude forests in North America and Europe, the seasonal trajectories of GOME-2 datasets were significantly correlated with GPP_{EC} with R^2 values ranged from 0.53 to 0.74 with the linear model, while that ranged from 0.76 to 0.86 with the hyperbolic model. At the same time, the start and end of growing seasons estimated by GOME-2 and OCO-2 SIF matched closely with EC based estimations. Among MODIS estimations, the SOS captured by NDVI and PI were most reliable estimations with the R^2 over 0.4. No MODIS indexes accurately predicted the EOS with an overall R^2 below 0.3.

Recently, data from OCO-2 has the great potentials in advancing the estimations of regional photosynthesis (Sun et al., 2017). However, we found that growing seasons estimated by OCO-2 SIF were relatively shorter than that of the EC-based estimations (up to 3 to 4 weeks) possibly due to the limited data from OCO-2 SIF for most sites. The limited observations from OCO-2 may lead its applications to be restrained at a small range of sites. Meanwhile, Tropospheric Monitoring Instrument (TROPOMI) that just recently launched on-board Sentinel-5 Precursor in October of 2017 and Fluorescence Explorer (Flex) scheduled to be launched around 2022 will start to provide global consistent observations soon. They will provide high-resolution global estimations of SIF (7 km by 7 km for TROPOMI and 300 m for Flex) that can be used to explore the potential of satellite-derived SIF in estimating photosynthetic capacity and seasonality (Alemohammad et al., 2016; Frankenberg et al., 2014; Guanter et al., 2015; Rascher et al., 2008). For Flex, the revisiting cycles repeat every 27 days, which may lead to a difficulty for retrieving seasonal patterns. But with the wider swath patterns, it can revisit the mid-to-high latitude regions up to every four days (Drusch et al., 2016).

Acknowledgments

This work was supported by the Chinese Arctic and Antarctic Administration, National Natural Science Foundation of China (Grant Nos. 41676176 and 41676182), the Chinese Polar Environment Comprehensive Investigation, Assessment Program (Grant No. 312231103). This work was also supported by the Fundamental Research Funds for the Central Universities. We acknowledge Dr. Köhler P. for sharing the satellite-derived SIF, Dr. Tramontana G. and Prof. M. Jung for providing the upscaled model GPP. The data of OCO-2 SIF was produced by the OCO-2 project at the Jet Propulsion Laboratory, California Institute of Technology, and obtained from the OCO-2 data archive maintained at the NASA Goddard Earth Science Data and Information Services Center. Eddy based canopy measurements are from European Fluxes Database Cluster (http://gaia.agraria.unitus.it/) and Fluxnet (http://fluxnet.fluxdata.org/); we would like to address our appreciation for the PIs and staff that are working on these sites. The study of US-Syv, US-PFa, and Us-WCr is found by Department of Energy Office of Science, Ameriflux Network Management Project Support

for UW ChEAS Cluster (2012-present). The study of US-Prr was supported by the JICS (JAMSTEC-UAF/IARC Collaboration Study).

References

Alemohammad, S.H., Fang, B., Konings, A.G., Green, J.K., Kolassa, J., Prigent, C., Aires, F., Miralles, D., Gentine, P., 2016. Water, Energy, and Carbon with Artificial Neural Networks (WECANN): A statistically-based estimate of global surface turbulent fluxes using solar-induced fluorescence. Biogeosciences Discussions, 1-36.

Attard, K.M., Hancke, K., Sejr, M.K., Glud, R.N., 2016. Benthic primary production and mineralization in a High Arctic fjord: in situ assessments by aquatic eddy covariance. Marine Ecology Progress Series 554, 35-50.

Badgley, G., Field, C.B., Berry, J.A., 2017. Canopy near-infrared reflectance and terrestrial photosynthesis. Science Advances 3, e1602244.

Baker, N.R., 2008. Chlorophyll fluorescence: a probe of photosynthesis in vivo. Annual Review of Plant Biology 59, 89-113.

Baldocchi, D., Falge, E., Gu, L., Olson, R., Hollinger, D., Running, S., Anthoni, P., Bernhofer, C., Davis, K., Evans, R., 2001. FLUXNET: A new tool to study the temporal and spatial variability of ecosystem-scale carbon dioxide, water vapor, and energy flux densities. Bulletin of the American Meteorological Society 82, 2415-2434.

Barr, A.G., Griffis, T.J., Black, T.A., Lee, X., Staebler, R.M., Fuentes, J.D., Chen, Z., Morgenstern, K., 2002. Comparing the carbon budgets of boreal and temperate deciduous forest stands. Canadian Journal of Forest Research 32, 813-822(810).

Beer, C., Reichstein, M., Tomelleri, E., Ciais, P., Jung, M., Carvalhais, N., Rödenbeck, C., Arain, M.A., Baldocchi, D., Bonan, G.B., 2010. Terrestrial gross carbon dioxide uptake: global distribution and covariation with climate. Science 329, 834-838.

Bergeron, O., Margolis, H.A., Black, T.A., Coursolle, C., Dunn, A.L., Barr, A.G., Wofsy, S.C., 2007. Comparison of carbon dioxide fluxes over three boreal black spruce forests in Canada. Global change biology 13, 89-107.

Bond-Lamberty, B., Wang, C., Gower, S.T., 2004. A global relationship between the heterotrophic and autotrophic components of soil respiration? Global change biology 10,

1756–1766.
Buitenwerf, R., Rose, L., Higgins, S.I., 2015. Three decades of multi-dimensional change in global leaf phenology. Nature Climate Change 5, 364-368.
Burrows, M.T., Schoeman, D.S., Buckley, L.B., Moore, P., Poloczanska, E.S., Brander, K.M., Brown, C., Bruno, J.F., Duarte, C.M., Halpern, B.S., 2011. The Pace of Shifting Climate in Marine and Terrestrial Ecosystems. Science 334, 652.
Chen, B., Coops, N.C., Fu, D., Margolis, H.A., Amiro, B.D., Black, T.A., Arain, M.A., Barr, A.G., Bourque, P.A., Flanagan, L.B., 2012. Characterizing spatial representativeness of flux tower eddy-covariance measurements across the Canadian Carbon Program Network using remote sensing and footprint analysis. Remote Sensing of Environment 124, 742-755.
Cleland, E.E., Chuine, I., Menzel, A., Mooney, H.A., Schwartz, M.D., 2007. Shifting plant phenology in response to global change. Trends in Ecology & Evolution 22, 357-365.
Cook, B.D., Davis, K.J., Wang, W.G., Desai, A., Berger, B.W., Teclaw, R.M., Martin, J.G., Bolstad, P.V., Bakwin, P.S., Yi, C.X., 2004. Carbon exchange and venting anomalies in an upland deciduous forest in northern Wisconsin, USA. Agricultural & Forest Meteorology 126, 271-295.
D'Odorico, P., Gonsamo, A., Gough, C.M., Bohrer, G., Morison, J., Wilkinson, M., Hanson, P.J., Gianelle, D., Fuentes, J.D., Buchmann, N., 2015a. The match and mismatch between photosynthesis and land surface phenology of deciduous forests. Agricultural & Forest Meteorology s 214–215, 25-38.
D'Odorico, P., Gonsamo, A., Gough, C.M., Bohrer, G., Morison, J., Wilkinson, M., Hanson, P.J., Gianelle, D., Fuentes, J.D., Buchmann, N., 2015b. The match and mismatch between photosynthesis and land surface phenology of deciduous forests. Agricultural and Forest Meteorology 214-215, 25-38.
Damm, A., Elbers, J., Erler, A., Gioli, B., Hamdi, K., Hutjes, R., Kosvancova, M., Meroni, M., Miglietta, F., Moersch, A., 2010. Remote sensing of sun-induced fluorescence to improve modeling of diurnal courses of gross primary production (GPP). Global Change Biology 16, 171-186.
Damm, A., Guanter, L., Paul-Limoges, E., Tol, C.V.D., Hueni, A., Buchmann, N., Eugster, W., Ammann, C., Schaepman, M.E., 2015. Far-red sun-induced chlorophyll fluorescence shows

509 ecosystem-specific relationships to gross primary production: An assessment based on
510 observational and modeling approaches. Remote Sensing of Environment 166, 91-105.
511 Delbart, N., Kergoat, L., Toan, T.L., Lhermitte, J., Picard, G., 2005. Determination of
512 phenological dates in boreal regions using normalized difference water index. Remote
513 Sensing of Environment 97, 26-38.
514 Desai, A.R., 2014. Influence and predictive capacity of climate anomalies on daily to decadal
515 extremes in canopy photosynthesis. Photosynthesis Research 119, 31-47.
516 Desai, A.R., Bolstad, P.V., Cook, B.D., Davis, K.J., Carey, E.V., 2005. Comparing net
517 ecosystem exchange of carbon dioxide between an old-growth and mature forest in the upper
518 Midwest, USA. Agricultural & Forest Meteorology 128, 33-55.
519 Dragoni, D., Schmid, H.P., Wayson, C.A., Potter, H., Csb, G., Randolph, J.C., 2011. Evidence
520 of increased net ecosystem productivity associated with a longer vegetated season in a
521 deciduous forest in south-central Indiana, USA. Global change biology 17, 886–897.
522 Drusch, M., Moreno, J., Bello, U.D., Franco, R., Goulas, Y., Huth, A., Kraft, S., Middleton,
523 E.M., Miglietta, F., Mohammed, G., 2016. The FLuorescence EXplorer Mission
524 Concept-ESA's Earth Explorer 8. IEEE Transactions on Geoscience & Remote Sensing PP,
525 1-12.
526 Frankenberg, C., O'Dell, C., Berry, J., Guanter, L., Joiner, J., Köhler, P., Pollock, R., Taylor,
527 T.E., 2014. Prospects for chlorophyll fluorescence remote sensing from the Orbiting Carbon
528 Observatory-2. Remote Sensing of Environment 147, 1-12.
529 Fretwell, P.T., Larue, M.A., Morin, P., Kooyman, G.L., Wienecke, B., Ratcliffe, N., Fox, A.J.,
530 Fleming, A.H., Porter, C., Trathan, P.N., 2012. An emperor penguin population estimate: the
531 first global, synoptic survey of a species from space. PLoS One 7, e33751.
532 Gonsamo, A., Chen, J.M., Price, D.T., Kurz, W.A., Wu, C., 2012a. Land surface phenology
533 from optical satellite measurement and CO2 eddy covariance technique. Journal of
534 Geophysical Research: Biogeosciences 117, n/a-n/a.
535 Gonsamo, A., Chen, J.M., Wu, C., Dragoni, D., 2012b. Predicting deciduous forest carbon
536 uptake phenology by upscaling FLUXNET measurements using remote sensing data.
537 Agricultural and Forest Meteorology 165, 127-135.
538 Guanter, L., Aben, I., Tol, P., Krijger, J.M., Hollstein, A., Köhler, P., Damm, A., Joiner, J.,

539 Frankenberg, C., Landgraf, J., 2015. Potential of the TROPOspheric Monitoring Instrument
540 (TROPOMI) onboard the Sentinel-5 Precursor for the monitoring of terrestrial chlorophyll
541 fluorescence. Atmospheric Measurement Techniques 8, 1337-1352.
542 Guanter, L., Rossini, M., Colombo, R., Meroni, M., Frankenberg, C., Lee, J.-E., Joiner, J.,
543 2013. Using field spectroscopy to assess the potential of statistical approaches for the
544 retrieval of sun-induced chlorophyll fluorescence from ground and space. Remote Sensing of
545 Environment 133, 52-61.
546 Guanter, L., Zhang, Y., Jung, M., Joiner, J., Voigt, M., Berry, J.A., Frankenberg, C., Huete,
547 A.R., Zarco-Tejada, P., Lee, J.E., Moran, M.S., Ponce-Campos, G., Beer, C., Camps-Valls, G.,
548 Buchmann, N., Gianelle, D., Klumpp, K., Cescatti, A., Baker, J.M., Griffis, T.J., 2014. Global
549 and time-resolved monitoring of crop photosynthesis with chlorophyll fluorescence. Proc
550 Natl Acad Sci U S A 111, E1327-1333.
551 Huete, A., Didan, K., Miura, T., Rodriguez, E.P., Gao, X., Ferreira, L.G., 2002. Overview of
552 the radiometric and biophysical performance of the MODIS vegetation indices. Remote
553 Sensing of Environment 83, 195-213.
554 Jeong, S.J., Schimel, D., Frankenberg, C., Drewry, D.T., Fisher, J.B., Verma, M., Berry, J.A.,
555 Lee, J.E., Joiner, J., 2017. Application of satellite solar-induced chlorophyll fluorescence to
556 understanding large-scale variations in vegetation phenology and function over northern high
557 latitude forests. Remote Sensing of Environment 190, 178-187.
558 Jin, C., Xiao, X., Wagle, P., Griffis, T., Dong, J., Wu, C., Qin, Y., Cook, D.R., 2015. Effects of
559 in-situ and reanalysis climate data on estimation of cropland gross primary production using
560 the Vegetation Photosynthesis Model. Agricultural and Forest Meteorology 213, 240-250.
561 Joiner, J., Guanter, L., Lindstrot, R., Voigt, M., Vasilkov, A.P., Middleton, E.M., Huemmrich,
562 K.F., Yoshida, Y., Frankenberg, C., 2013. Global monitoring of terrestrial chlorophyll
563 fluorescence from moderate-spectral-resolution near-infrared satellite measurements:
564 methodology, simulations, and application to GOME-2. Atmospheric Measurement
565 Techniques 6, 2803-2823.
566 Joiner, J., Yoshida, Y., Guanter, L., Middleton, E.M., 2016. New methods for retrieval of
567 chlorophyll red fluorescence from hyper-spectral satellite instruments: simulations and
568 application to GOME-2 and SCIAMACHY. Atmospheric Measurement Techniques

569 Discussions, 1-41.
570 Joiner, J., Yoshida, Y., Vasilkov, A.P., Schaefer, K., Jung, M., Guanter, L., Zhang, Y., Garrity,
571 S., Middleton, E.M., Huemmrich, K.F., Gu, L., Belelli Marchesini, L., 2014. The seasonal
572 cycle of satellite chlorophyll fluorescence observations and its relationship to vegetation
573 phenology and ecosystem atmosphere carbon exchange. Remote Sensing of Environment 152,
574 375-391.
575 Jung, M., Reichstein, M., Bondeau, A., 2009. Towards global empirical upscaling of
576 FLUXNET eddy covariance observations: validation of a model tree ensemble approach
577 using a biosphere model. Biogeosciences 6, 2001-2013.
578 Jung, M., Reichstein, M., Margolis, H.A., Cescatti, A., Richardson, A.D., Arain, M.A., Arneth,
579 A., Bernhofer, C., Bonal, D., Chen, J., 2011. Global patterns of land-atmosphere fluxes of
580 carbon dioxide, latent heat, and sensible heat derived from eddy covariance, satellite, and
581 meteorological observations. Journal of Geophysical Research Biogeosciences 116, 245-255.
582 Köhler, P., Guanter, L., Joiner, J., 2015. A linear method for the retrieval of sun-induced
583 chlorophyll fluorescence from GOME-2 and SCIAMACHY data. Atmospheric Measurement
584 Techniques 8, 2589-2608.
585 Köhler, P., Guanter, L., Kobayashi, H., Walther, S., Yang, W., 2017. Assessing the potential of
586 sun-induced fluorescence and the canopy scattering coefficient to track large-scale vegetation
587 dynamics in Amazon forests. Remote Sensing of Environment.
588 Kurz, W.A., Apps, M.J., Stocks, B.J., Jan, Volney, A., 1995. Global Climate Change:
589 Disturbance Regimes and Biospheric Feedbacks of Temperate and Boreal Forests.
590 Li, X., Xiao, J., He, B., 2017. Chlorophyll fluorescence observed by OCO-2 is strongly
591 related to gross primary productivity estimated from flux towers in temperate forests. Remote
592 Sensing of Environment.
593 Liu, Z., Wu, C., Peng, D., Wang, S., Gonsamo, A., Fang, B., Yuan, W., 2017. Improved
594 modeling of gross primary production from a better representation of photosynthetic
595 components in vegetation canopy. Agricultural & Forest Meteorology 233, 222-234.
596 Loveland, T.R., Reed, B.C., Brown, J.F., Ohlen, D.O., Zhu, Z., Yang, L., Merchant, J.W.,
597 2000. Development of a global land cover characteristics database and IGBP DISCover from
598 1 km AVHRR data. International Journal of Remote Sensing 21, 1303-1330.

599 Lu, X., Xiao, C., Xianglan, L., Tang, J., 2018. Opportunities and challenges of applications of
600 satellite-derived sun-induced fluorescence at relatively high spatial resolution. Science of the
601 Total Environment 619-620C, 649-653.
602 Luo, X., Chen, X., Wang, L., Xu, L., Tian, Y., 2014. Modeling and predicting spring land
603 surface phenology of the deciduous broadleaf forest in northern China. Agricultural & Forest
604 Meteorology 198-199, 33-41.
605 Luus, K.A., Commane, R., Parazoo, N.C., Benmergui, J., Euskirchen, E.S., Frankenberg, C.,
606 Joiner, J., Lindaas, J., Miller, C.E., Oechel, W.C., Zona, D., Wofsy, S., Lin, J.C., 2017. Tundra
607 photosynthesis captured by satellite-observed solar-induced chlorophyll fluorescence.
608 Geophysical Research Letters 44, 1564-1573.
609 Marcolla, B., Pitacco, A., Cescatti, A., 2003. Canopy Architecture and Turbulence Structure
610 in a Coniferous Forest. Boundary-Layer Meteorology 108, 39-59.
611 Mccaughey, J.H., Pejam, M.R., Arain, M.A., Cameron, D.A., 2006. Carbon dioxide and
612 energy fluxes from a boreal mixedwood forest ecosystem in Ontario, Canada. Agricultural &
613 Forest Meteorology 140, 79-96.
614 Milyukova, I.M., Kolle, O., Varlagin, A.V., Vygodskaya, N.N., Schulze, E.D., Lloyd, J., 2002.
615 Carbon balance of a southern taiga spruce stand in European Russia. Tellus 54, 429-442.
616 Myneni, R.B., Hoffman, S., Knyazikhin, Y., Privette, J.L., Glassy, J., Tian, Y., Wang, Y., Song,
617 X., Zhang, Y., Smith, G.R., 2002. Global products of vegetation leaf area and fraction
618 absorbed PAR from year one of MODIS data. Remote Sensing of Environment 83, 214-231.
619 Nakai, T., Kim, Y., Busey, R.C., Suzuki, R., Nagai, S., Kobayashi, H., Park, H., Sugiura, K.,
620 Ito, A., 2013. Characteristics of evapotranspiration from a permafrost black spruce forest in
621 interior Alaska. Polar Science 7, 136-148.
622 Peng, D., Wu, C., Li, C., Zhang, X., Liu, Z., Ye, H., Luo, S., Liu, X., Hu, Y., Fang, B., 2017.
623 Spring green-up phenology products derived from MODIS NDVI and EVI: Intercomparison,
624 interpretation and validation using National Phenology Network and AmeriFlux observations.
625 Ecological Indicators 77, 323-336.
626 Peñuelas, J., Rutishauser, T., Filella, I., 2009. Phenology Feedbacks on Climate Change.
627 Science 324, 887-888.
628 Press, W.H., Teukolsky, S.A., Vetterling, W.T., Flannery, B.P., Numerical recipes in C.

629 Rascher, U., Gioli, B., Miglietta, F., 2008. FLEX — Fluorescence Explorer: A Remote
630 Sensing Approach to Quantify Spatio-Temporal Variations of Photosynthetic Efficiency from
631 Space. Springer Netherlands.
632 Reichstein, M., Falge, E., Baldocchi, D., Papale, D., Aubinet, M., Berbigier, P., Bernhofer, C.,
633 Buchmann, N., Gilmanov, T., Granier, A., 2005. On the separation of net ecosystem exchange
634 into assimilation and ecosystem respiration: review and improved algorithm. Global change
635 biology 11, 1424-1439.
636 Rolleston, H.D., 1996. Influence of the temperate and boreal forests on the Northern
637 Hemisphere climate in the Météo-France climate model. Climate Dynamics 13, 57-74.
638 Rouse, J.W., Haas, R.W., Schell, J.A., Deering, D.W., Harlan, J.C., 1974. Monitoring the
639 vernal advancement and retrogradation (Greenwave effect) of natural vegetation.
640 NASA/GSFCT Type III final report. Nasa.
641 Sims, D.A., Rahman, A.F., Cordova, V.D., El-Masri, B.Z., Baldocchi, D.D., Bolstad, P.V.,
642 Flanagan, L.B., Goldstein, A.H., Hollinger, D.Y., Misson, L., 2008. A new model of gross
643 primary productivity for North American ecosystems based solely on the enhanced vegetation
644 index and land surface temperature from MODIS. Remote Sensing of Environment 112,
645 1633-1646.
646 Staudt, K., Foken, T., 2008. Documentation of reference data for the experimental areas of
647 the Bayreuth Centre for Ecology and Environmental Research (BayCEER) at the Waldstein
648 site.
649 Sulkava, M., Luyssaert, S., Zaehle, S., Papale, D., 2015. Assessing and improving the
650 representativeness of monitoring networks: The European flux tower network example.
651 Journal of Geophysical Research Biogeosciences 116, 278-278.
652 Sun, Y., Frankenberg, C., Wood, J.D., Schimel, D.S., Jung, M., Guanter, L., Drewry, D.T.,
653 Verma, M., Porcar-Castell, A., Griffis, T.J., 2017. OCO-2 advances photosynthesis
654 observation from space via solar-induced chlorophyll fluorescence. Science 358, eaam5747.
655 Suni, T., Rinne, J., Reissell, A., Al, E., 2003. Long-term measurements of surface fluxes
656 above a Scot pine forest in Hyytiälä southern Finland, 1996-2001. Boreal Environment
657 Research 8, 287-301.
658 Tang, J., Körner, C., Muraoka, H., Piao, S., Shen, M., Thackeray, S.J., Yang, X., 2016.

659 Emerging opportunities and challenges in phenology: a review. Ecosphere 7, e01436.
660 Tanja, S., Berninger, F., Vesala, T., Markkanen, T., Hari, P., Mäkelä, A., Ilvesniemi, H.,
661 Hänninen, H., Nikinmaa, E., Huttula, T., 2003. Air temperature triggers the recovery of
662 evergreen boreal forest photosynthesis in spring. Global change biology 9, 1410–1426.
663 Tramontana, G., Jung, M., Schwalm, C.R., Ichii, K., Campsvalls, G., Ráduly, B., Reichstein,
664 M., Altaf Arain, M., Cescatti, A., Kiely, G., 2016. Predicting carbon dioxide and energy
665 fluxes across global FLUXNET sites with regression algorithms. Biogeosciences Discussions
666 13, 1-33.
667 Turner, D.P., Ritts, W.D., Cohen, W.B., Gower, S.T., Zhao, M., Running, S.W., Wofsy, S.C.,
668 Urbanski, S., Dunn, A.L., Munger, J.W., 2003. Scaling Gross Primary Production (GPP) over
669 boreal and deciduous forest landscapes in support of MODIS GPP product validation.
670 Remote Sensing of Environment 88, 256-270.
671 Urbanski, S., Barford, C., Wofsy, S., Kucharik, C., Pyle, E., Budney, J., Mckain, K.,
672 Fitzjarrald, D., Czikowsky, M., Munger, J.W., 2007. Factors controlling CO2 exchange on
673 timescales from hourly to decadal at Harvard Forest. Journal of Geophysical Research
674 Biogeosciences 112, 225-236.
675 van der Tol, C., Berry, J.A., Campbell, P.K., Rascher, U., 2014. Models of fluorescence and
676 photosynthesis for interpreting measurements of solar-induced chlorophyll fluorescence. J
677 Geophys Res Biogeosci 119, 2312-2327.
678 Verma, M., Schimel, D., Evans, B., Frankenberg, C., Beringer, J., Drewry, D.T., Magney, T.,
679 Marang, I., Hutley, L., Moore, C., 2017. Effect of environmental conditions on the
680 relationship between solar-induced fluorescence and gross primary productivity at an OzFlux
681 grassland site. Journal of Geophysical Research Biogeosciences 122.
682 Viña, A., Liu, W., Zhou, S., Huang, J., Liu, J., 2016. Land surface phenology as an indicator
683 of biodiversity patterns. Ecological Indicators 64, 281-288.
684 Walther, S., Voigt, M., Thum, T., Gonsamo, A., Zhang, Y., Kohler, P., Jung, M., Varlagin, A.,
685 Guanter, L., 2016. Satellite chlorophyll fluorescence measurements reveal large-scale
686 decoupling of photosynthesis and greenness dynamics in boreal evergreen forests. Glob
687 Chang Biol 22, 2979-2996.
688 Wang, C., Cao, R., Chen, J., Rao, Y., Tang, Y., 2015. Temperature sensitivity of spring

689 vegetation phenology correlates to within-spring warming speed over the Northern
690 Hemisphere. Ecological Indicators 50, 62-68.
691 Wong, C.Y., Gamon, J.A., 2015. The photochemical reflectance index provides an optical
692 indicator of spring photosynthetic activation in evergreen conifers. New Phytologist 206, 196.
693 Wu, C., Peng, D., Soudani, K., Siebicke, L., Gough, C.M., Arain, M.A., Bohrer, G., Lafleur,
694 P.M., Peichl, M., Gonsamo, A., Xu, S., Fang, B., Ge, Q., 2017. Land surface phenology
695 derived from normalized difference vegetation index (NDVI) at global FLUXNET sites.
696 Agricultural and Forest Meteorology 233, 171-182.
697 Xiao, X., Hollinger, D., Aber, J., Goltz, M., Davidson, E.A., Zhang, Q., Iii, B.M., 2004a.
698 Satellite-based modeling of gross primary production in an evergreen needleleaf forest.
699 Remote Sensing of Environment 89, 519-534.
700 Xiao, X., Zhang, Q., Braswell, B., Urbanski, S., Boles, S., Wofsy, S., Iii, B.M., Ojima, D.,
701 2004b. Modeling gross primary production of temperate deciduous broadleaf forest using
702 satellite images and climate data. Remote Sensing of Environment 91, 256-270.
703 Yang, H., Yang, X., Zhang, Y., Heskel, M.A., Lu, X., Munger, J.W., Sun, S., Tang, J., 2017.
704 Chlorophyll fluorescence tracks seasonal variations of photosynthesis from leaf to canopy in
705 a temperate forest. Global change biology 23, 2874-2886.
706 Yang, X., Tang, J., Mustard, J.F., Lee, J.E., Rossini, M., Joiner, J., Munger, J.W., Kornfeld, A.,
707 Richardson, A.D., 2015. Solar-induced chlorophyll fluorescence that correlates with canopy
708 photosynthesis on diurnal and seasonal scales in a temperate deciduous forest. Geophysical
709 Research Letters 42, 2977-2987.
710 Yang, X., Tang, J., Mustard, J.F., Wu, J., Zhao, K., Serbin, S., Lee, J.-E., 2016. Seasonal
711 variability of multiple leaf traits captured by leaf spectroscopy at two temperate deciduous
712 forests. Remote Sensing of Environment 179, 1-12.
713 Zhang, Y., Guanter, L., Berry, J.A., van der Tol, C., Yang, X., Tang, J., Zhang, F., 2016a.
714 Model-based analysis of the relationship between sun-induced chlorophyll fluorescence and
715 gross primary production for remote sensing applications. Remote Sensing of Environment
716 187, 145-155.
717 Zhang, Y., Xiao, X., Jin, C., Dong, J., Zhou, S., Wagle, P., Joiner, J., Guanter, L., Zhang, Y.,
718 Zhang, G., Qin, Y., Wang, J., Moore, B., 2016b. Consistency between sun-induced

719 chlorophyll fluorescence and gross primary production of vegetation in North America.
720 Remote Sensing of Environment 183, 154-169.
721 Zhang, Y., Xiao, X., Zhang, Y., Wolf, S., Zhou, S., Joiner, J., Guanter, L., Verma, M., Sun, Y.,
722 Yang, X., 2018. On the relationship between sub-daily instantaneous and daily total gross
723 primary production: Implications for interpreting satellite-based SIF retrievals. Remote
724 Sensing of Environment 205.
725